Journal of ELECTRONIC MATERIALS, Vol. 33, No. 6, 2004 *Special Issue Paper*

Spectral Crosstalk by Radiative Recombination in Sequential-Mode, Dual Mid-Wavelength Infrared Band HgCdTe Detectors

R.A. COUSSA,[1] A.M. GALLAGHER,[1] K. KOSAI,[1,4] L.T. PHAM,[1]
G.K. PIERCE,[1] E.P. SMITH,[1] G.M. VENZOR,[1] T.J. DE LYON,[2] J.E. JENSEN,[2]
B.Z. NOSHO,[2] J.A. ROTH,[2] and J.R. WATERMAN[3]

1.—Raytheon Vision Systems, Goleta, CA 93117. 2.—HRL Laboratories LLC, Malibu, CA 90265.
3.—Naval Research Laboratory, Washington, DC 20375. 4.—E-mail: kkosai@raytheon.com

For small pixel, infrared (IR) focal plane arrays (FPAs), Raytheon Vision Systems' architecture for integrated, dual-band detectors uses the sequential mode of the n-p^+-n configuration. There is a single indium bump per pixel, leaving the p^+ layer floating, and the operating polarity of the bias selects the spectral sensitivity by reverse-biasing the active p-n junction. Photogenerated minority carriers in the absorber layer of the forward-biased inactive photodiode are lost through recombination. This paper is the first report of a new optical crosstalk mechanism that occurs in sequential-mode, dual-band detectors. In the long-wavelength mode under out-of-band, short-wavelength illumination, radiative recombination yields emission near the bandgap energy of the short-wavelength absorber layer, resulting in a spurious short-wavelength response that appears as spectral crosstalk. We present experimental and device modeling results on the spectral crosstalk in molecular-beam-epitaxy-grown HgCdTe arrays with the cutoff wavelength of both bands in the 4–5-µm range.

Key words: HgCdTe, infrared detector, two-color detector, crosstalk, radiative recombination

INTRODUCTION

Compared with a single-band sensor, multispectral capability in a military infrared (IR) imaging system for target searching and identification offers advantages that include longer-range enhanced detection and recognition of obscured or camouflaged objects and improved rejection of clutter. The conventional approach uses a beam splitter and multiple focal plane arrays (FPAs) and results in increased size, weight, and power consumption. A detector FPA that monolithically integrates the multispectral sensing not only overcomes these penalties, but also gives automatic registration of the pixels, higher reliability, simpler manufacturing, and lower cost.

One approach to a monolithic, dual-band detector array is the vertical integration of two p^+-n photodiodes in which the optical absorption occurs in the n-type layers.[1] Inverting the long-wavelength detector into an n-p^+ device that is grown on top of the shorter band device and merging the p^+ layers integrates the two photodiodes in an n-p^+-n heterostructure. Operated in a backside-illuminated configuration, the first n-type layer absorbs the shorter wavelength (Band 1) radiation, which is sensed by the bottom photodiode. Longer wavelength (Band 2) radiation passes through the bottom n-type absorber and middle p^+ layer to be detected by the top photodiode.

When indium-bump bonded to a silicon readout integrated circuit (ROIC), this architecture requires two electrical contacts within each unit cell: one to the top longer-wave n-type layer and the second to the middle p^+ layer. The third contact is to the bottom n-type layer, which is common to all pixels, and is made outside the unit cell near the perimeter of the array. Because both photodiodes in each pixel operate independently and sense radiation at the same time, this architecture is referred to as a simultaneous-mode, dual-band FPA.[2]

The simultaneous-mode approach is difficult to scale to pixels with dimensions on the order of 35 µm or less. The two electrical contacts and indium bumps

(Received September 17, 2003; accepted January 20, 2004)

result in the effective optical area of the Band-2 detector decreasing faster than the pixel size as the pixel shrinks because of the more complicated photolithographic processing associated with the extreme topography of small-area mesas having heights in the range of 10–15 μm. In addition, twice the circuitry, one readout for each band, must fit in the unit cell of the ROIC, which may require compromises in overall performance because of space limitations.

Because of its better scalability to small pixels, Raytheon prefers the sequential-mode detector in which the central p^+ layer is left electrically floating and electrical contact is made within the unit cell only to the Band-2 n-type layer.[2–5] The tradeoff is that only one detector can be operating at any given time, with the active photodiode being selected by the polarity of the bias. Among the advantages are Band-2 optical areas approaching 100% of the pixel, simpler photolithographic processing, and an ROIC unit cell similar to that in a single-band FPA. For example, sequential-mode detector arrays have been hybridized to a single-band readout and used for imaging in a conventional camera.

The structure of the simultaneous and sequential architectures is depicted in Fig. 1a. The principal difference between the two is the presence in the simultaneous device of an ohmic contact to the middle p-type layer that is shared by the two diodes. We also represent the two p-n junctions as back-to-back diodes in the electrical schematic in the right side of Fig. 1a. The graph of Fig. 1b displays typical doping and composition profiles. Instead of CdTe fraction, x, in $Hg_{1-x}Cd_xTe$, we have represented the composition as the optical wavelength in micrometers, λ_G, equivalent to the bandgap energy in electron volts at 90 K, $E_G = 1.24/\lambda_G$. Infrared radiation incident on the detector through the substrate is absorbed in the bottom Band-1 absorber layer if its wavelength is shorter than the Band-1 cutoff wavelength, λ_{C1}. Radiation with wavelength longer than λ_{C1}, but shorter than λ_{C2}, the Band-2 cutoff, passes through the short-wavelength IR, composition p-type layer and is absorbed in the top absorber layer.

As discussed in previous papers,[2,4,5] the spectral band of the sequential-mode detector is selected by choosing the voltage applied to the Band-2 contact such that the active photodiode is reverse-biased, and the inactive is forward-biased. The reverse-biased diode collects the holes photogenerated in its absorber layer, and the resulting photocurrent, as well as the active-diode dark current, flows through the forward-biased junction of the inactive detector. Because the inactive photodiode is forward-biased, holes generated in its absorber layer are not collected. The carriers injected by the forward-biased junction and the photogeneration in the inactive diode result in an increase of the hole concentration, which, in steady state, must be balanced by recombination. This process includes nonradiative mechanisms, such as Shockley–Read–Hall (SRH) recombination through impurity centers and Auger recombination, as well as band-to-band and other radiative channels.

This model is complicated by the fact that the n-p^+-n structure is the same as a bipolar junction transistor and can exhibit gain, especially in the Band-2 mode.[2,4] Methods of suppressing the gain are to incorporate energy barriers in the p^+ layer that inhibit electron transport and to reduce electron injection by the forward-biased junction. Electron injection can be minimized by making the acceptor concentration in the p-type layer large compared with the donor density in both n-type layers and placing heterojunctions at the p-n junctions to make the built-in voltages for electrons larger than for holes.

In this paper, we present the first report of a new spectral-crosstalk mechanism in which photons generated by radiative recombination of Band-1 photocarriers give a spurious signal in the Band-2 mode. This mechanism does not give crosstalk in the Band-1 mode because radiative recombination in the Band-2 n-type layer creates photons below the

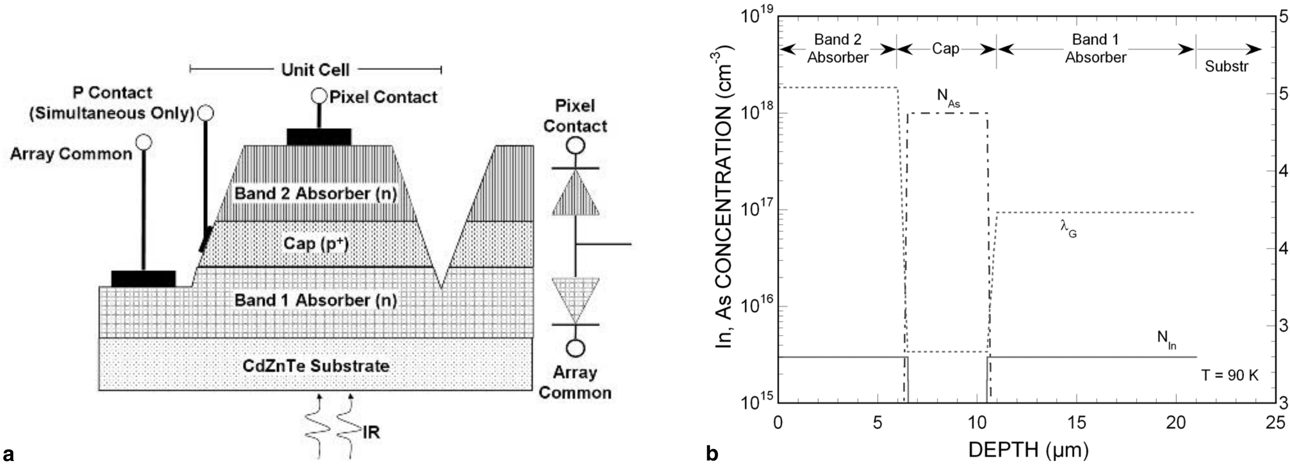

Fig. 1. (a) Cross section and layers of the simultaneous and sequential dual-band architectures and the corresponding electrical schematic. (b) Typical doping and composition profiles of the device, where alloy composition has been represented on the right axis as an optical wavelength corresponding to the bandgap energy.

bandgap energy of the Band-1 absorber layer. In the following sections, we discuss experimental and device simulation results for HgCdTe dual-band detectors with the cutoff wavelengths of both bands in the 4–5-µm range.

EXPERIMENTAL

The HgCdTe layers for simultaneous- and sequential-mode devices were grown by molecular-beam epitaxy on CdZnTe substrates at HRL Laboratories LLC (Malibu, CA).[5–7] The layers were doped during growth with indium as the donor species, and arsenic as the acceptor. Typical structures consist of a 10-µm-thick, Band-1 n-type layer with 3×10^{15} cm^{-3} indium concentration; 5-µm-thick, p-type layer with 10^{18} arsenic density; and a 6-µm, Band-2 n-type layer having 3×10^{15} indium (Fig. 1b). The CdTe fraction, x, in the bottom Band-1 absorber layer is approximately 0.34, while the composition of the top Band-2 layer is near 0.30. At a temperature of 90 K, these compositions correspond to a Band-1 cutoff wavelength of 4 µm, and a Band-2 cutoff of 5 µm. The p-type layer has the same composition as the Band-1 absorber in the simultaneous-mode devices. In the sequential-mode devices, the p-type layer contains an energy barrier with the maximum x near 0.38 to suppress electron transport that contributes to transistor gain.

Detectors were photolithographically delineated using an anisotropic dry-etch technique to form mesas about 12 µm in height and passivated with CdTe. All measurements were made on representative test-structure die containing isolated devices and 10 × 10 arrays of various pixel sizes and designs. For testing, individual die were indium-bump bonded to passive carriers with electrical leads for contacting sample devices. Detector spectral characteristics were measured using a Fourier-transform IR spectrometer.

All of the experimental data presented here were taken at temperatures for which the dark current is not measurable with our test apparatus. Values of dark current were below 1 picoampere and believed to be at least a factor of 100 below currents flowing under illumination.

Figure 2a shows the spectral-quantum response at 78 K, normalized to a peak value of unity, of a simultaneous-mode detector in a 10 × 10 array with 40-µm pixel size. Cutoff wavelength, defined as the point at which the quantum response is 50% of the peak, is 4.19 µm in the Band-1 mode and 5.18 in the Band-2 mode. The solid curve (i) is the response measured with the Band-2 contact biased −50 mV relative to the common Band 1, and the middle p-type layer left floating (Band-1 sequential mode). The two dashed curves are the response in the Band-2 mode with +150-mV bias and the p-layer left floating (curve (ii), sequential mode, alternating long and short dashed line) and shorted to the Band-1 contact at ground potential (curve (iii), simultaneous mode, short dashed line). Figure 2b gives electrical schematic diagrams of the bias configurations for the three curves in the graph.

The most important feature of Fig. 2a is the twice larger Band-2 mode response at wavelengths below 4 µm with the p-type layer floating instead of grounded. We attribute this additional signal to the top photodiode sensing the emission created by the radiative recombination of the photogenerated carriers in the Band-1 absorber layer and will concentrate on this phenomenon in the remainder of the paper.

To be complete, we briefly note two anomalies in Fig. 2a. The first is the large response to wavelengths shorter than 4 µm in the simultaneous Band-2 photodiode, curve (iii). The simultaneous-mode, Band-2 response to wavelengths less than 4 µm should be zero, assuming all such radiation

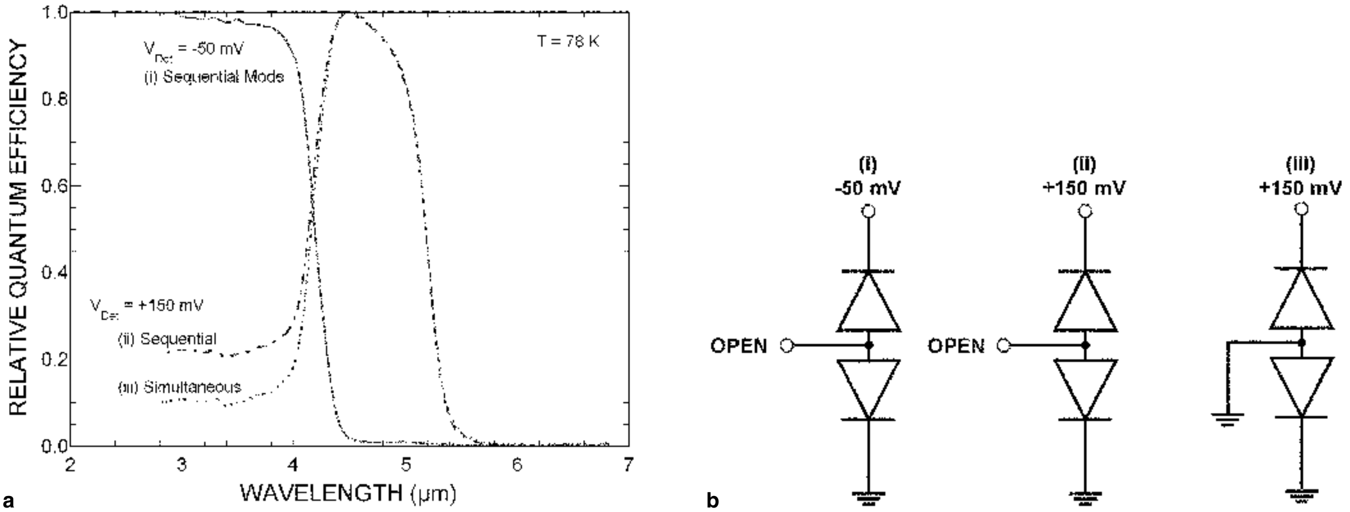

Fig. 2. (a) Relative quantum efficiency of simultaneous dual-band detector biased in (i) short-wavelength (solid line) and long-wavelength (dashed) modes with (ii) p-layer floating (sequential) or (iii) biased (simultaneous). A floating p layer results in higher short-wavelength response in the Band-2 mode. (b) Electrical schematic showing the bias arrangements at which the curves in the graph were measured.

is absorbed by the Band-1 photodiode. The large response in the simultaneous mode of Fig. 2a is believed to be due to the test condition in which the contacts of the neighboring detectors were left open. As a consequence of the photogenerated holes in the surrounding Band-1 absorber layers not being collected, there could have been significant radiative recombination that was sensed by the test device. The second anomaly is the small response around 5 μm in the Band-1 sequential-mode of curve (i); this may be due to transistor gain or unknown test artifacts arising from the adjacent floating detectors. Transistor gain is possible because the devices were intended for simultaneous operation, and the design of the HgCdTe doping and composition profiles did not incorporate features to suppress it. The cause of the structure was not determined, but it is believed to be unrelated to the central topic of spectral crosstalk arising from radiative recombination.

To confirm the existence of luminescence caused by radiative recombination, we measured the current-voltage characteristics of a pixel, operated with the p-type layer floating, at several discrete values of the forward-bias voltage on the Band-1 diode of an adjacent pixel, as schematically illustrated in Fig. 3a. The bias across the Band-2 diode of the adjacent pixel was held at zero by shorting the Band-2 n-type contact to the p-type. Figure 3b shows the results, where each curve represents a different forward bias on the adjacent diode.

The interpretation of the data is complicated by the parasitic, lateral PNP (p-type, n-type, p-type) transistor in which the forward-biased diode acts as the emitter; the reverse-biased, Band-1 p-n junction in the sequential detector as the collector; and the bottom n-type layer as the base. For positive bias across the sequential detector, both bottom diodes are forward-biased, disabling the lateral PNP transistor, and the variation of the saturation current with forward bias on the adjacent Band-1 diode is a result of the Band-2 diode in the sequential detector sensing radiation emitted by the adjacent Band-1 p-n junction. With negative bias across the sequential detector, the lateral PNP transistor is active, and the saturation current has two components. The first is proportional to the holes injected into the shared n-type layer, and the second is a function of the luminescence emitted by the forward-biased diode.

A different test structure, containing only sequential-mode detectors, exhibits behavior that is best interpreted as detection of radiative recombination. The wafer in which these detectors were fabricated was engineered for sequential-mode operation and has an energy barrier in the p-type layer to suppress transistor gain. The measurements were taken on a group of 3 × 3 diodes within a larger 10 × 10 array. Figure 4a schematically indicates the electrical connections for the measurement of the spectral response of the central pixel that was recorded at several fixed values of the bias applied to seven of the eight surrounding pixels. One of the corner pixels in the 3 × 3 group was inaccessible because of the configuration of the fanout.

As shown in Fig. 4b, the central pixel, when operated in Band-2 mode at +150-mV bias, has a response at wavelengths shorter than 4.2 μm that depends on the bias of the surrounding pixels and is additive with the intrinsic spectral crosstalk arising within the test detector. The additional response is at a minimum when the surrounding pixels are biased at −500 mV and increases as the bias is changed to zero, then +500 mV. This is qualitatively consistent with the expected amount of hole current and luminescence by Band-1 diodes in the surrounding pixels. Photogenerated holes in these pixels are most efficiently collected at −500-mV bias, yielding the least radiative recombination; inefficiently collected at zero bias; and not collected at +500, giving maximum luminescence.

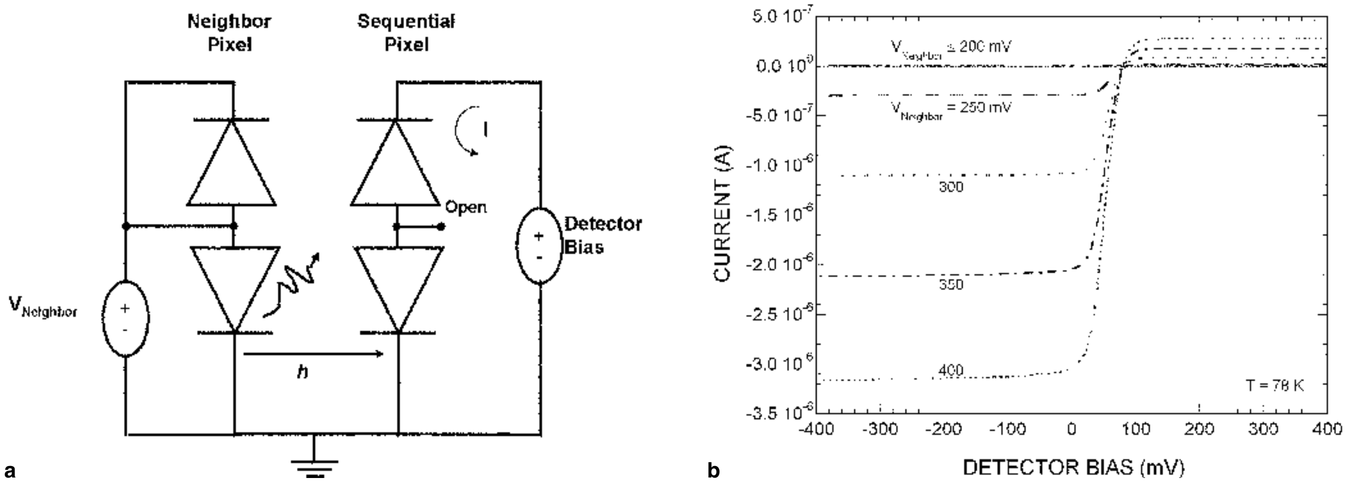

Fig. 3. (a) Electrical schematic for measurement of the current-voltage curves of a dual-band, sequential-mode detector at several fixed values of the forward bias on the Band-1 diode of an adjacent pixel. (b) The positive-bias saturation current depends on the bias of the adjacent Band-1 diode, showing it emits radiation.

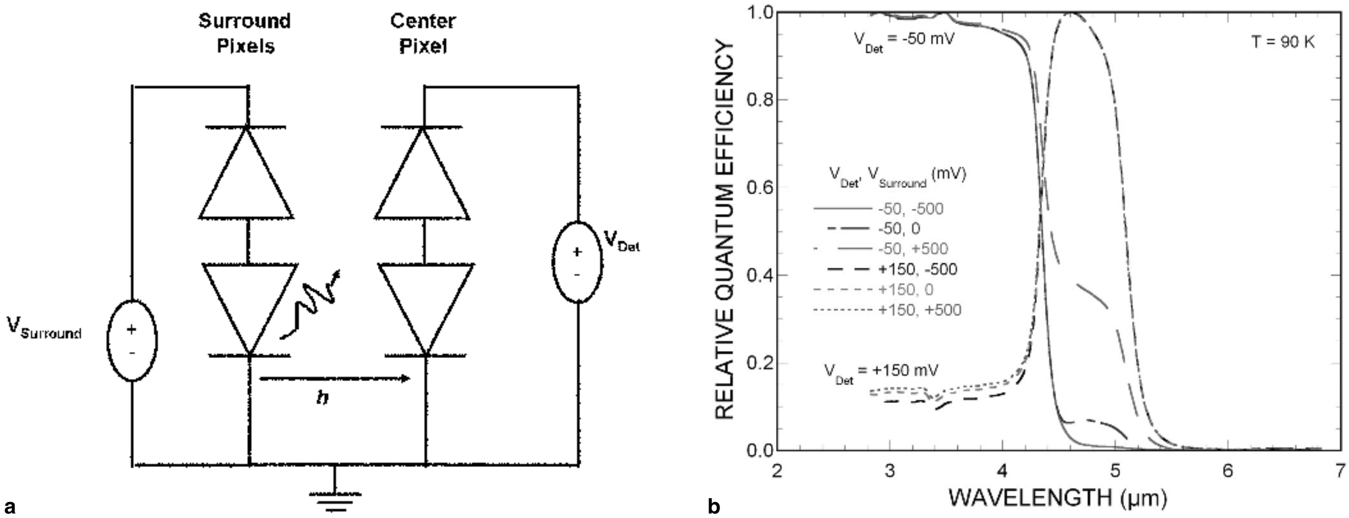

Fig. 4. (a) Schematic diagram for measurement and (b) spectral response of a sequential detector in Band 1 and 2 modes at discrete values of the bias on seven of the surrounding eight detectors. All curves are normalized such that each has a peak value of unity.

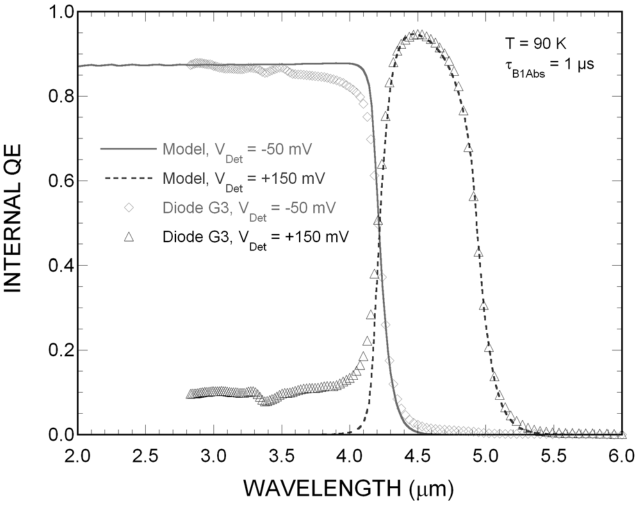

Fig. 5. Modeled (lines) and experimental (symbols) spectral-quantum response of a sequential-mode detector.

The central-pixel Band-1 response, taken at a bias of −50 mV, exhibits a long-wavelength shoulder beyond the cutoff that we attribute to lateral diffusion of holes originating from the surrounding pixels. The magnitude of the shoulder is consistent with the dependence of hole injection on surrounding detector bias, being highest at positive bias and lowest at negative. The shoulder also depends on the photocurrent in the surrounding pixels, which is proportional to the incident Band-2 photon flux.

DEVICE MODELING

This section discusses one-dimensional calculations using the commercial device simulator Dessis,[8] as well as the internally developed model Het III.[9] Both of these models solve the coupled set of equations consisting of Poisson's and the drift-diffusion equations for electrons and holes.[9] Doping and composition profiles for the simulations were obtained from secondary ion mass spectrometry (SIMS) measurements by Charles Evans and Associates (Sunnyvale, CA) taken on part of a sequential-mode wafer after completion of device processing. All of the results in this section are from a single wafer that is different from those of the preceding section, although identical in design to the sequential-mode device of Fig. 4.

The primary SIMS ion was Cs^+ for the composition and arsenic profiles and O_2^- for indium. The SIMS composition profile was corrected for the composition dependence of the sputter rate,[10] and the raw and uncorrected depths were used as a lookup table to adjust the depth scales for arsenic and indium.

To smooth the SIMS data and improve the numerical stability of the device simulations, analytic representations of the composition and doping profiles were obtained by fitting each to a sum of error functions. To correct for the error of the SIMS measurement, the composition profile was scaled, according to the equation:

$$x_{Scaled} = 1.055(x - 0.315) \qquad (1)$$

where the numerical values in Eq. 1 were chosen to force the model spectral response to fit the experimental, as shown in Fig. 5. The measured spectral response for each band, represented by the symbols, was scaled to have the same peak value as that calculated by the model. Cutoff wavelengths are 4.2 µm for Band 1 and 4.9 µm for Band 2.

Model recombination mechanisms were band-to-band radiative and SRH, given by:

$$U_{Rad} = B\left(np - n_i^2\right) \qquad (2)$$

for radiative and

$$U_{SRH} = \frac{np - n_i^2}{\tau_{p0}\left(n + n_1\right) + \tau_{n0}\left(p + p_1\right)} \qquad (3)$$

for SRH. Equations 2 and 3 follow the notation and variable definitions of Reine et al.[11] The radiative

Table I. Mobilities and SRH Lifetime Parameters for Device Simulations

Layer	μ_n (cm^2/V·s)	μ_p (cm^2/V·s)	τ_{SRH} (µs)
Band-1 absorber	3×10^4	500	1, 2, 5
p-Type middle	6×10^3	200	0.05
Band-2 absorber	3×10^4	500	1

coefficient, B, depends on the temperature and local composition, while the SRH trap energy was taken to be at the local, intrinsic Fermi level. The optical absorption coefficient was calculated using the composition- and temperature-dependent expressions of Hougen.[12]

For an indium concentration of 3×10^{15} cm^{-3} and a composition of 0.33 in the Band-1 absorber layer, the calculated lifetime caused by radiative recombination is 1.7 µs at a temperature of 90 K. The Auger 1 recombination lifetime[11] is estimated to be 24 µs for the same parameters. Based on the measured Band-1 quantum efficiencies, the nonradiative lifetime was inferred to be in the 1–5-µsec range and modeled with the SRH mechanism. The Auger 1 recombination was omitted from device simulations because of its large lifetime compared with radiative and SRH.

Table I lists the values of mobility and SRH lifetime parameters, which were assumed to be constant within each of the three layers. The electron and hole SRH-lifetime parameters, τ_{n0} and τ_{p0}, were equal with the values listed in Table I.

The simulators do not account for the reabsorption of the photons generated by the radiative recombination. Dumke[13] has shown that the effect of reabsorption is to redistribute the photogenerated carriers with an effective diffusivity given by

$$D = \frac{1}{3\tau_{\mathrm{Rad}}\left\langle \alpha^2 \right\rangle} \tag{4}$$

where τ_{Rad} is the radiative lifetime, and $\langle \alpha^2 \rangle$ is the value of the squared absorption coefficient averaged over the energy of the emitted photons. Assuming 1.7 µs for the radiative lifetime and 2.5×10^5 cm^{-2} for the absorption coefficient factor, Eq. 4 gives a value of 0.78 cm^2/s for D, which at 90 K corresponds to an effective mobility of 100 cm^2/V·s, 20% of the model hole mobility (Table I). This shows that the redistribution effects of photon reabsorption are relatively small compared to carrier diffusion.

Simulated current-voltage characteristics are shown in Fig. 6 for no illumination (solid curve, labeled "$\Phi = 0$") and with a photon flux of 10^{15} cm^{-2} s^{-1} at wavelengths of 4 µm and 4.5 µm (dashed curves annotated with wavelength). The curves with illumination represent the total simulated current, which includes the dark-current leakage. The dips in the curves are the points at which the current changes from negative on the left side to positive on the right. Under illumination, the portion of a curve in which the detector is inactive is the right side for the 4-µm wavelength case and the left for the 4.5 µm. The current under this condition is a result of the small amount of above-cutoff, 4.5-µm radiation absorbed by the Band-1 detector in the longer wavelength case. For the shorter wavelength case, the Band-2 mode current for biases greater than 0.09 V is a consequence of the residual IR not absorbed by the Band-1 n-type layer. In both cases, the out-of-band response corresponds to detecting a fraction equal to 5×10^{-3} of the incident flux and is probably accurate to an order of magnitude because of numerical errors of the discretized model.

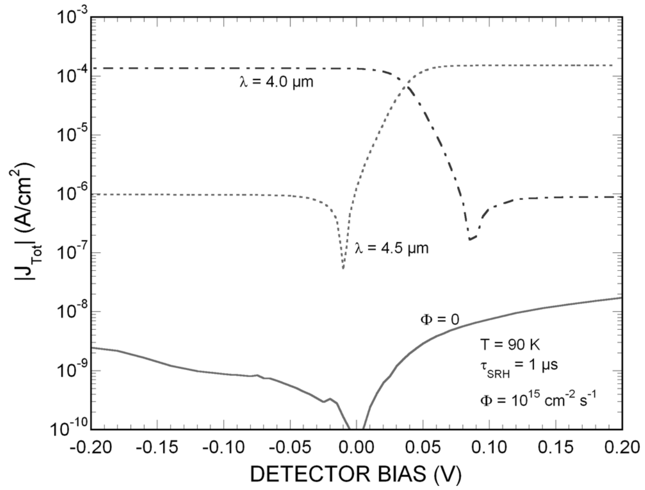

Fig. 6. Simulated current-voltage curves with no IR illumination (solid curve) and 10^{15} cm^{-2}·s^{-1} illumination at wavelengths of 4 µm and 4.5 µm (dashed lines).

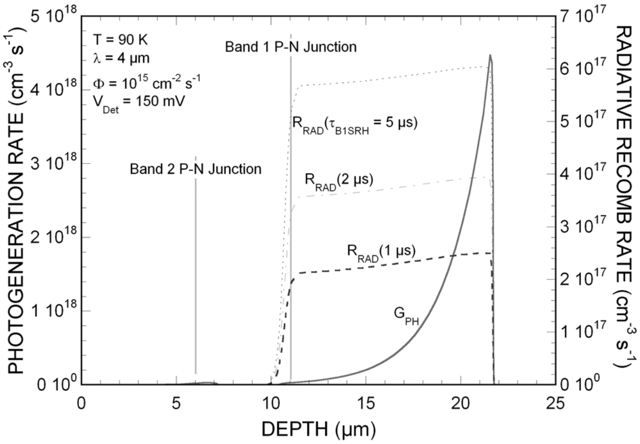

Fig. 7. Simulated photogeneration (solid line) and radiative-recombination (dashed) rates with SRH lifetime in the Band-1 absorber layer as a parameter. Detector biased in long-wavelength mode under short-wavelength illumination.

Figure 7 is a plot showing the spatial distribution of the simulated radiative-recombination rate at 150-mV bias (Band-2 detection mode) under a Band-1 photon flux of 10^{15} cm^{-2}·s^{-1} and 4-µm wavelength. There are three dashed curves corresponding to SRH lifetimes in the Band-1 absorber layer of 1 µs, 2 µs, and 5 µs. As a reference, Fig. 7 also plots the photogeneration rate (solid line) and indicates the position of the two p-n junctions. The radiative-recombination rate is nearly constant within the Band-2 absorber layer as a result of diffusion and also increases with increasing SRH lifetime. In all cases, there is a small contribution to the radiative-recombination rate from holes injected by the forward-biased Band-1 p-n junction, but it is negligible as shown by the 4-μm current-voltage curve in Fig. 6.

Assuming that half the photons are emitted toward the Band-2 diode, which detects them with 100% efficiency, the spatially integrated radiative-recombination rate, normalized to twice the input photon flux, is an upper bound on the quantum response of the detector in Band-2 mode to out-of-band radiation. As shown by the middle curve in Fig. 8, the parameter varies between 0.13 and 0.32 as the Band-1 SRH lifetime changes from 1 μs to 5 μs. As a comparison, the Band-1 internal quantum efficiency at 4 μm is in the range of 0.86 to 0.96 (top curve, Fig. 8).

A more accurate estimate of the Band-2 response to Band-1 radiation is

$$\eta_{21} = \frac{1}{2\Phi}\int_0^L R(z)\exp\left(-\int_0^z \alpha(u)\,du\right)dz \approx \frac{\int_0^L R(z)dz}{2\Phi}\frac{1}{\alpha L}\left(1-e^{-\alpha L}\right) \tag{5}$$

where Φ is the input photon flux, R is the radiative-recombination rate, L is the thickness of the Band-1 absorber, and α is the absorption coefficient. The second half of Eq. 5 follows from the first by assuming that R has a constant value equal to its integrated value divided by L and that α is constant. This expression is applicable for a single photon energy, and a more accurate treatment would account for the spectral distribution of the radiative recombination.

Assuming that the radiative recombination results in a photon energy equal to the bandgap, a CdTe fraction of 0.3296 and a temperature of 90 K gives 446 cm^{-1} for the absorption coefficient at 0.2924 eV.[12] Together with 11 μm for L and the normalized, integrated values of R/2 in Fig. 8, Eq. 5 gives values of 0.10, 0.16, and 0.24 for η_{21}, which are plotted as the bottom curve in Fig. 8. These values differ by less than a factor of 2 from the measured crosstalk value of 0.17, defined as the quantum response at a wavelength of 4 μm, divided by the peak, in-band response (Fig. 5). This calculation suggests that the SRH lifetime in the Band-1 absorber layer is on the order of 2 μs.

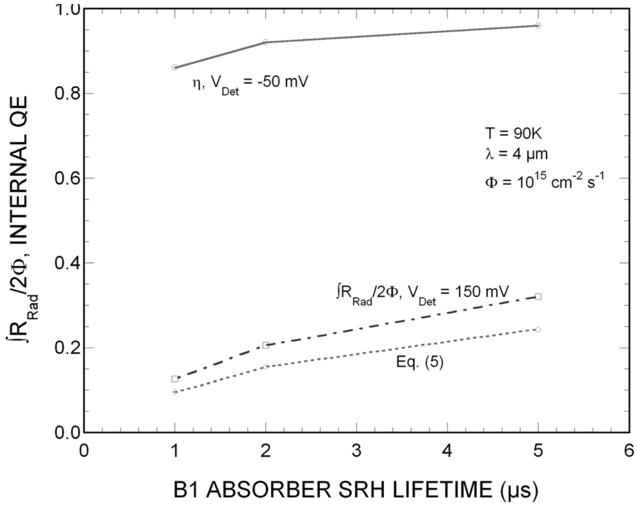

Fig. 8. Calculated quantum response to radiation at 4 μm in Band-1 mode (solid line) and two estimates of Band-2 quantum response to 4-μm radiation (dashed) as a function of SRH lifetime.

DISCUSSION

In this section, we examine the amount of recombination that occurs by band-to-band radiative recombination, its dependence on doping density, as well as including the effects of Auger 1 recombination. The reasoning is independent of the magnitude of the photogeneration rate, and only depends on the relative magnitudes of the radiative, Auger 1, and SRH lifetimes as they vary with doping. In addition, we assume that the SRH lifetime is independent of the donor concentration in the Band-1 absorber layer. In the following, when we refer to Auger recombination, it is to be understood that we are referring to the Auger 1 mechanism.[11]

The amount of recombination that occurs radiatively, as a fraction of the total (radiative plus nonradiative) recombination, is related to the radiative and net nonradiative lifetimes by

$$\frac{R_{\text{Rad}}}{R_{\text{Tot}}}(N_D) = \frac{\dfrac{1}{\tau_{\text{Rad}}(N_D)}}{\dfrac{1}{\tau_{\text{Rad}}(N_D)}+\dfrac{1}{\tau_{\text{NR}}(N_D)}} \tag{6}$$

where R is a recombination rate, τ is a lifetime; and N_D is the donor concentration. Subscript Rad indicates radiative; Tot indicates total, which is the sum of radiative and nonradiative processes; and NR indicates nonradiative.

We express the N_D dependence of the radiative and Auger lifetimes in terms of their values at a fixed donor concentration, $N_{D,\text{Ref}}$, by

$$\tau_{\text{Rad}}(N_D) = \left(\frac{N_{D,\text{Ref}}}{N_D}\right)\tau_{\text{Rad,Ref}} \tag{7a}$$

$$\tau_A(N_D) = \left(\frac{N_{D,\text{Ref}}}{N_D}\right)^2 \tau_{A,\text{Ref}} \tag{7b}$$

The Ref subscript denotes the values of radiative and Auger lifetimes at the reference donor concentration. The net nonradiative-recombination lifetime caused by Auger and SRH recombination is

$$\tau_{\text{NR}} = \frac{1}{\dfrac{1}{\tau_A(N_D)}+\dfrac{1}{\tau_{\text{SRH}}}} \tag{8}$$

Inserting Eqs. 7 and 8 into Eq. 6 gives

$$\frac{R_{\mathrm{Rad}}}{R_{\mathrm{Tot}}}(N_D) = \frac{N_D \dfrac{\tau_{\mathrm{SRH}}}{\tau_{\mathrm{Rad,Ref}}}}{1 + N_D \dfrac{\tau_{\mathrm{SRH}}}{\tau_{\mathrm{Rad,Ref}}} + N_D^2 \dfrac{\tau_{\mathrm{SRH}}}{\tau_{\mathrm{A,Ref}}}} \tag{9}$$

According to Eq. 9, the radiative-recombination fraction approaches zero for both small and large values of N_D. At small values of N_D, the relative amount of radiative recombination becomes small because the radiative-recombination rate itself goes to zero, proportional to N_D. At large values of N_D, most of the recombination occurs as Auger recombination, and the fractional radiative recombination goes to zero as $1/N_D$. The radiative-recombination fraction has a maximum at an intermediate value, given by

$$N_{\mathrm{D,Max}} = N_{\mathrm{D,Ref}} \sqrt{\frac{\tau_{\mathrm{A,Ref}}}{\tau_{\mathrm{SRH}}}} \tag{10}$$

which follows by setting the derivative with respect to N_D of Eq. 9 to zero and solving for $N_{\mathrm{D,Max}}$.

Figure 9 plots the lifetimes given by Eqs. 7 and 8 and the fractional radiative-recombination rate defined in Eq. 9 for a temperature of 90 K, Band-1 absorber composition of 0.3296, and SRH lifetime of 1 μs. In addition, we have plotted the internal quantum efficiency for a wavelength of 4 μm and a hole mobility of 500 $\mathrm{cm^2/V\cdot s}$, as computed using Eq. 73 of Reine et al.[11] for a backside-illuminated photodiode. The curves in Fig. 9 show that the crosstalk caused by radiative recombination is best reduced by lowering the doping in the Band-1 absorber layer because the quantum efficiency decreases with higher donor concentration. Decreasing the donor concentration from 3×10^{15} to $10^{15}\ \mathrm{cm^{-3}}$ lowers the fractional radiative-recombination rate from 0.36 to 0.16, a ratio of 2.2, with a slight increase in quantum efficiency. To effect the same change by increasing the donor density requires that N_D be raised above 2×10^{17}, at which level the quantum efficiency is 0.01.

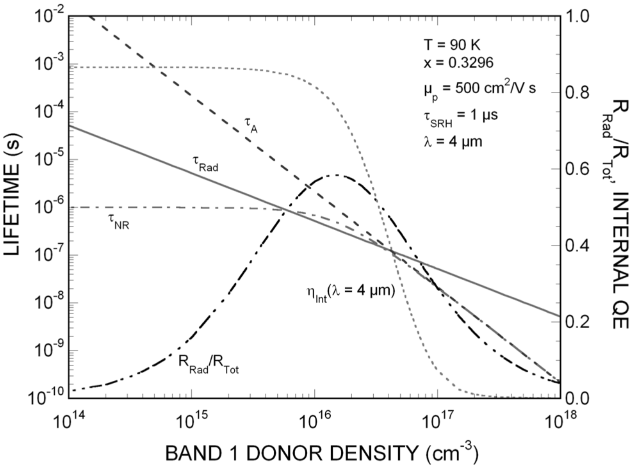

Fig. 9. Dependence of radiative (τ_{Rad}), Auger 1 (τ_A), and net nonradiative (τ_{NR}) lifetimes on donor concentration in the Band-1 absorber layer is plotted on the left axis. The ratio of radiative recombination to total recombination rate ($R_{\mathrm{Rad}}/R_{\mathrm{Tot}}$) and internal quantum efficiency at 4 μm (η_{Int}) are graphed using the right axis.

CONCLUSIONS

We have presented evidence for spectral crosstalk caused by radiative recombination in sequential-mode, dual-band HgCdTe detectors. In the Band-2 detection mode under Band-1 illumination, photogenerated carriers in the Band-1 absorber layer recombine radiatively and emit photons that are detected by the Band-2 photodiode. Although neglecting the reabsorption of the emitted photons, one-dimensional device simulation calculates a radiative-recombination rate that can be used to estimate the crosstalk within a factor of 2. A more accurate device simulation should include reabsorption, the spectral distribution of the radiative-recombination emission, and geometrical effects. Treating geometrical effects in the modeling of the reabsorption requires that the simulation be performed in three dimensions.

A simple calculation of the dependence of the radiative and Auger 1 recombination rates on donor density in the Band-1 absorber shows that the radiative recombination, as a fraction of the total recombination, has a maximum when N_D is $1.5 \times 10^{16}\ \mathrm{cm^{-3}}$ for the case in which $x = 0.33$, the SRH lifetime is 1 μs, and the Auger 1 lifetime is 24 μs at $N_D = 3 \times 10^{15}$. This simple model assumed that the only radiative mechanism is band-to-band recombination, and nonradiative recombination occurred only by SRH and Auger 1. Of course, there are many other radiative and nonradiative mechanisms that could be included. Among the radiative are free-to-bound and excitonic transitions.[14] A nonradiative mechanism that can be important in actual devices is surface recombination, which would require a two- or three-dimensional device simulation.

We have observed, as shown by the experimental data of Figs. 2–4, that radiative recombination can also be a source of optical crosstalk between neighboring pixels when all unit cells are not in the same bias condition. Such an operating condition is not normal in an active FPA but could be present in experiments similar to those discussed here.

ACKNOWLEDGEMENTS

This work was funded under Contract MSA-0032 ITO No. 01 from the Pennsylvania State Applied Research Center, Electrooptical Center, Office of Naval Research. J.R. Waterman of the Naval Research Laboratory is contract monitor. We also thank the reviewer, M.B. Reine, for his careful critique of the manuscript and cogent suggestions.

REFERENCES

1. J.C. Campbell, T.P. Lee, A.G. Dentai, and C.A. Burrus, *Appl. Phys. Lett.* 34, 401 (1979).
2. A. Rogalski, *Infrared Phys. Tech.* 41, 213 (2000).
3. E.F. Schulte, U.S. patent 5,113,076 (12 May 1992).
4. E.R. Blazejewski, J.M. Arias, G.M. Williams, W. McLevige, M. Zandian, and J. Pasko, *J. Vac. Sci. Technol. B* 10, 1626 (1992).
5. T.J. de Lyon, J.A. Vigil, O.K. Wu, J.L. Johnson, E.A. Patten, K. Kosai, G. Venzor, V. Lee, and S.M. Johnson, *J. Vac. Sci Technol. B* 16, 1321 (1998).

6. R.D. Rajavel et al., *J. Electron. Mater.* 26, 476 (1997).
7. R.D. Rajavel et al., *J. Electron. Mater.* 27, 747 (1998).
8. ISE Integrated Systems Engineering AG, Zurich.
9. K. Kosai, *J. Electron. Mater.* 24, 635 (1995).
10. J. Sheng, L. Wang, G.E. Lux, and Y. Gao, *J. Electron. Mater*. 26, 588 (1997).
11. M.B. Reine, A.K. Sood, and T.J. Tredwell, *Semiconductors and Semimetals*, Vol. 18, eds. R.K. Willardson and A.C. Beer (New York: Academic, 1981), pp. 201–311.
12. C.A. Hougen, *J. Appl. Phys.* 66, 3763 (1989).
13. W.P. Dumke, *Phys. Rev.* 105, 139 (1957).
14. J.I. Pankove, *Optical Processes in Semiconductors* (Englewood Cliffs, NJ: Prentice-Hall, 1971), pp. 107–159.